Supplementary Information – On the measurement of S$_{\text{diff}}$ splitting caused by
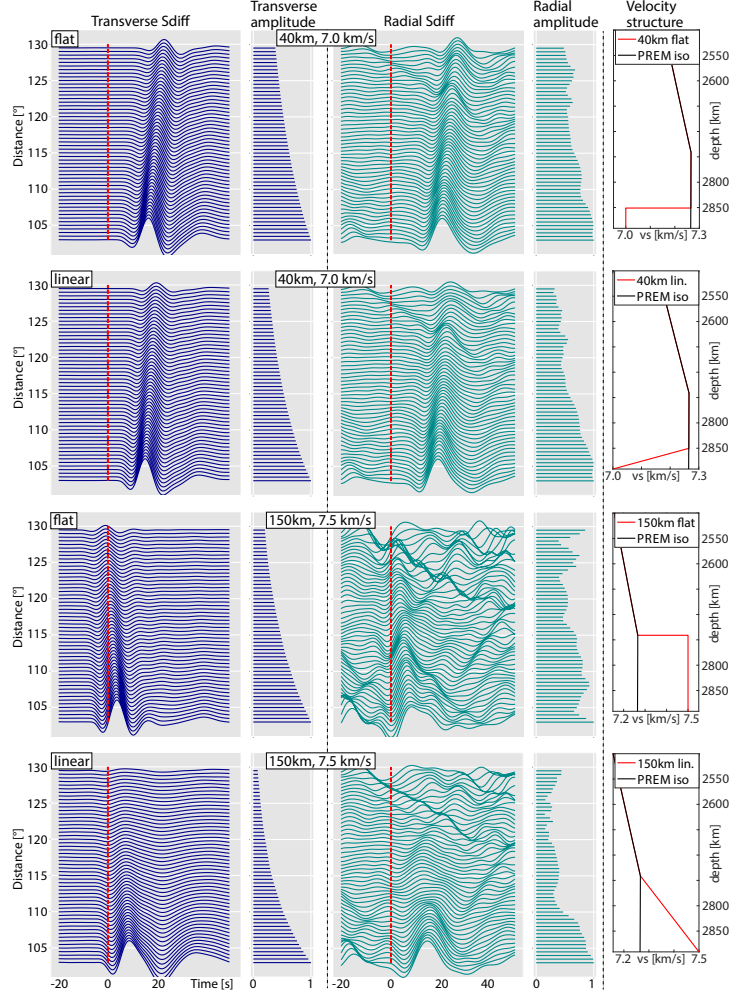
lowermost mantle anisotropy

Figure S1: Representation of the transverse (left column, dark blue) and radial (third column, teal) S$_{\text{diff}}$ waveforms as a function of epicentral distance. Transverse (second column, dark blue) and radial (fourth column, teal) amplitudes are also shown. S$_{\text{diff}}$ arrival times predicted by PREM are represented as red dashed lines. Waveforms are shown for four cases that all use isotropic PREM as their background model. Top row: 40 km thick layer at the base of the mantle with shear wave speeds of 7.0 $\frac{\text{km}}{\text{s}}$ (right column); second row: velocity of 7.0 $\frac{\text{km}}{\text{s}}$ at the base of the mantle and a linear gradient to PREM-like velocities 40 km above the CMB (right column); third row: 150 km thick layer at the base of the mantle with shear wave speeds of 7.5 $\frac{\text{km}}{\text{s}}$ (see right column); bottom row: and a velocity of 7.5 $\frac{\text{km}}{\text{s}}$ at the base of the mantle and a linear gradient gradient to PREM-like velocities 150 km above the CMB (see right column).
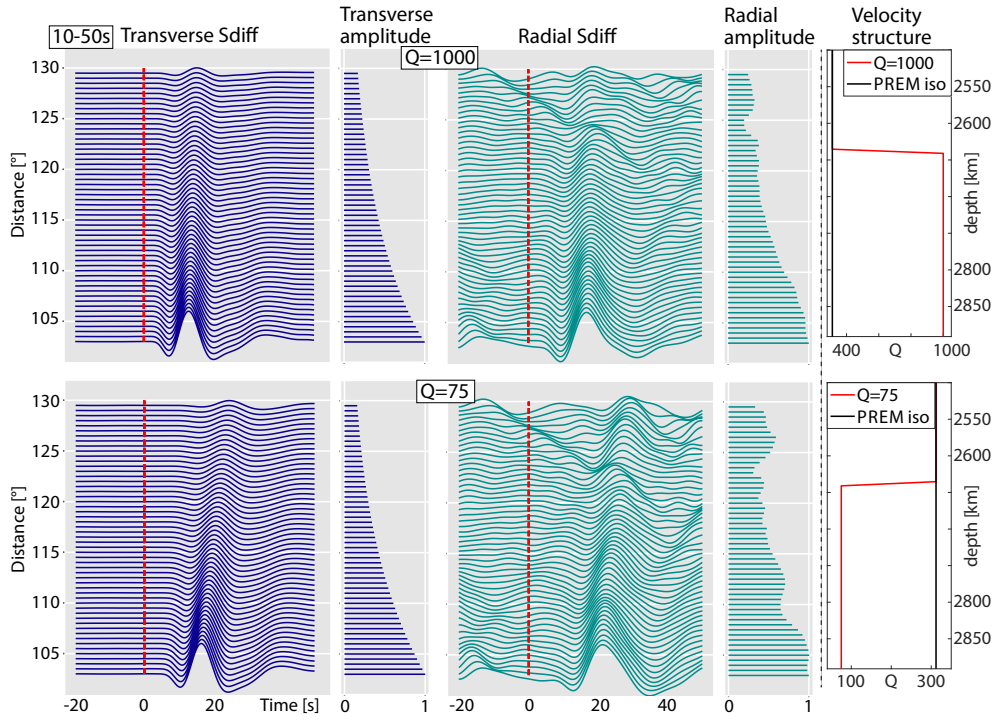
Figure S2: Transverse and radial S$_{\text{diff}}$ waveforms and amplitudes for shear quality factor values Q_μ (throughout this work called Q) of 1000 (upper and third row) and 75 (second and bottom row) in the lowermost mantle. Waveforms were bandpass-filtered, retaining frequencies between $10 - 50\,\text{s}$. Plotting conventions are the same as in Figure S1.
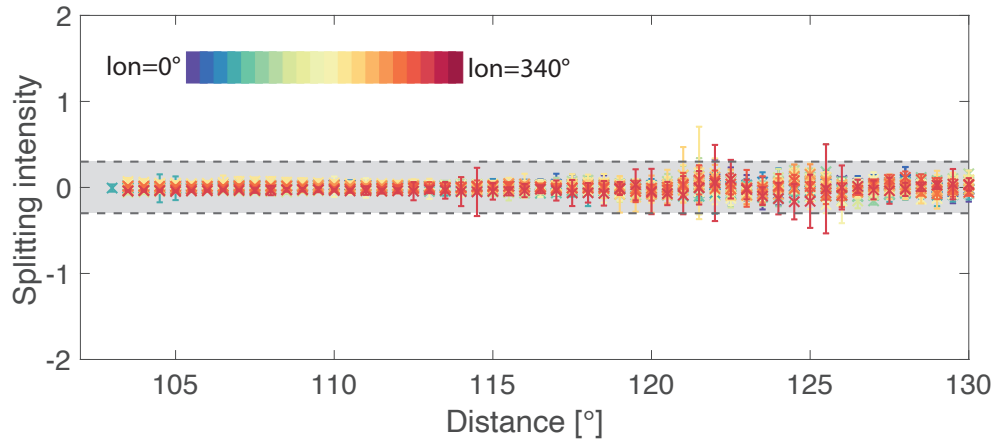

Figure S3: Splitting intensities as a function of distance for analogue source-receiver configurations along different longitudes (with a spacing of 20°; see legend). All splitting intensity measurements are null ($|SI| < -0.3$; indicated by black dashed lines). This figure is similar to Figure 5b of the main manuscript. The only difference is that S40RTS was used instead of GyPSuM.
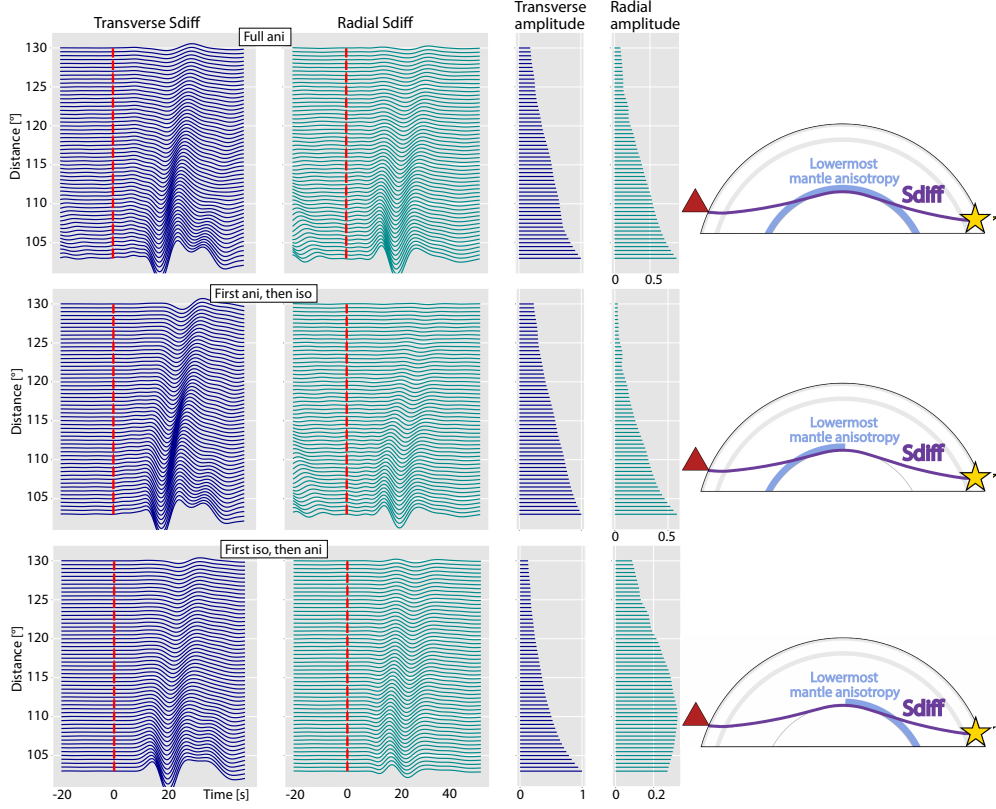
Figure S4: Similar to Figure 6 of the main manuscript using the GyPSuM tomography model for the mantle. Transverse and radial S_{diff} waveforms (columns 1, 2) and corresponding amplitudes (columns 3, 4) are shown for three different scenarios. These different scenarios are schematically illustrated in the right column, that shows raypaths (violet) from source (yellow star) to receiver (red triangle), and the location of the lowermost mantle anisotropy (light blue). Upper row: for a full global layer of Ppv anisotropy (represented by light blue color in right column); middle row: Lowermost mantle anisotropy, incorporated in the deep mantle up to an epicentral distance of 65° measured from the source (see right column); bottom row: from an epicentral distance of 65° from the source (see right column).
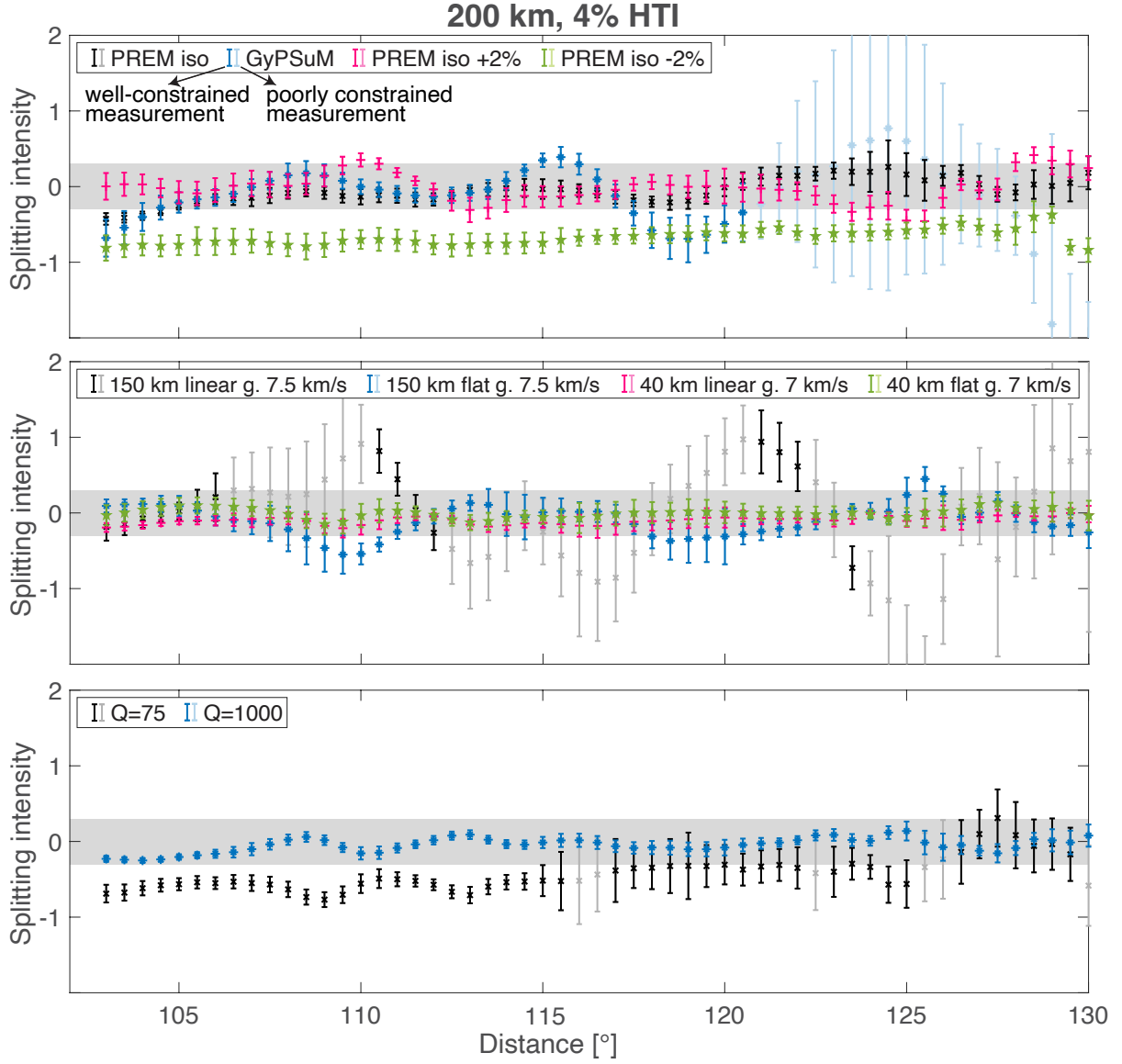
Figure S5: Results from similar simulations as those shown in Figure 8 of the main manuscript but for strong upper mantle anisotropy, plotted as SH_{diff} splitting intensities as a function of distance, calculated for a focal depth of 500 km. SI was measured using SplitRacer. 95% confidence intervals are indicated by error bars. Simulations for which the lowermost mantle velocity was modified are shown in the top panel. These include an input model for which the mantle in PREM has been replaced by the GyPSuM tomographic model (see legend). The middle panel shows results for different lowermost mantle velocity gradients, in particular, linear and flat gradients were tested (see legend). The bottom row presents results for two endmember Q-values. The shaded gray area indicates SI-values between -0.3 and 0.3, which would usually be defined as null.
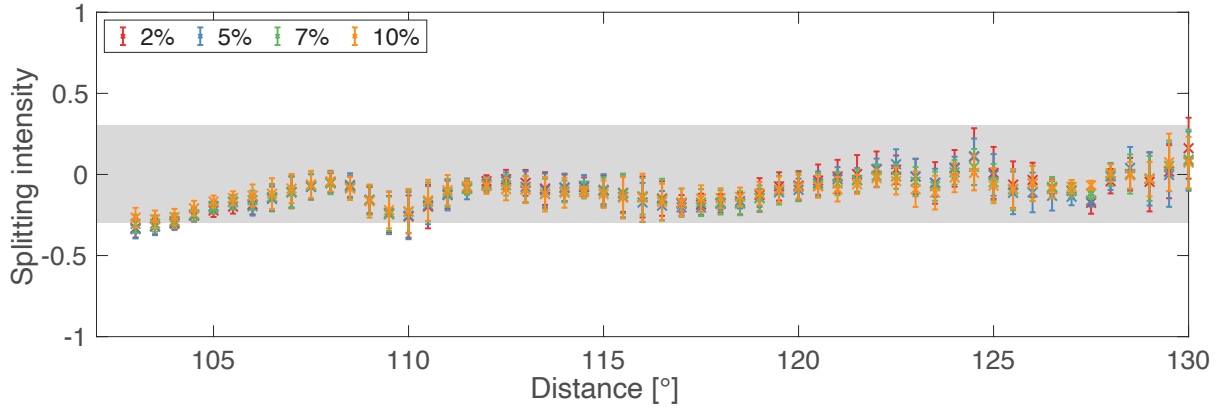
Figure S6: Similar to Figure 9 of the main manuscript for strong upper mantle anisotropy. Simulation results, expressed as measured splitting intensities, for initially SH-polarized S_{diff} waves for two different velocity reductions at the base of the mantle, calculated for a focal depth of $500\,km$. Plotting conventions are similar to Figure S9. Synthetics were computed for a $20\,km$ thick low velocity at the base of the mantle. P wave velocity reductions are $1/3$ of the S wave velocity reductions (see legend). 95% confidence intervals are shown by error bars. Almost all of the measurements are null. Results for other velocity reductions than those shown here are presented in Supplementary Figure S5.
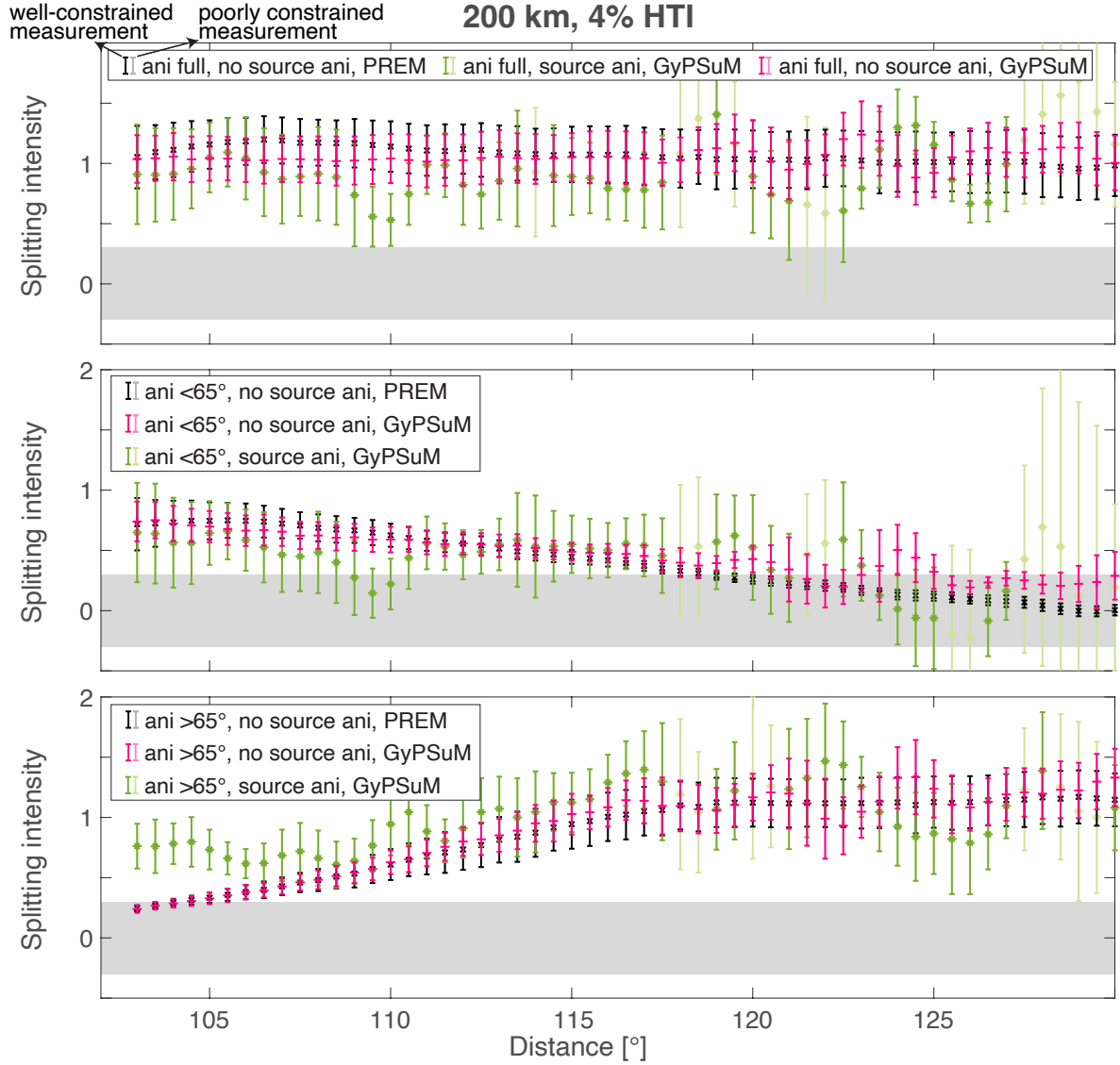
Figure S7: Similar to Figure 10 of the main manuscript for strong upper mantle anisotropy. Lowermost mantle anisotropy is incorporated for a full global layer of Ppv anisotropy, up to an epicentral distance of 65° (from the source) or from an epicentral distance of 65° (see legend). All simulations that use an isotropic PREM without GyPSuM include lowermost mantle anisotropy only (see legend). Simulations with GyPSuM tomography in the mantle (replacing PREM velocity structure) include source and receiver side anisotropy (see legend).
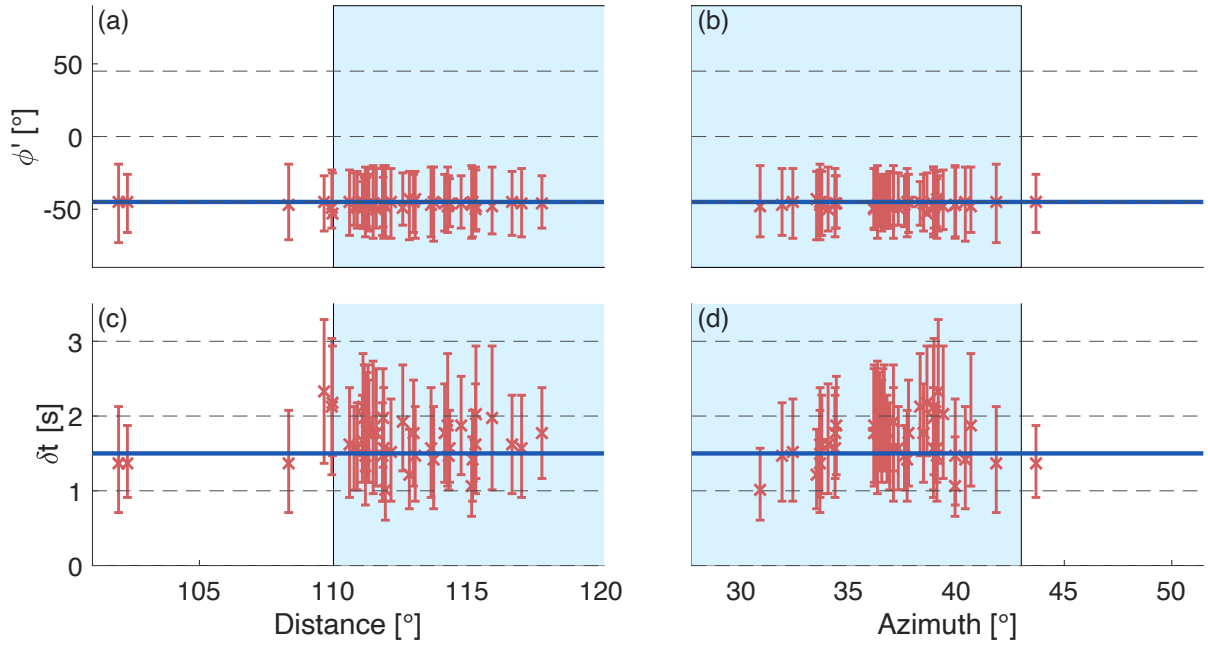
6

Figure S8: Well-constrained single station splitting parameters (ϕ', δt) for event 2009-10-04. (a-b) ϕ' as a function of (a) distance and (b) azimuth. Red markers show best fitting fast polarization directions determined using SplitRacer; 95% confidence intervals are presented as error bars. The blue line shows the best fitting fast polarization direction measured from the stacked S_{diff} waveform from this event. Light blue shading indicates distances > 110° and azimuths < 43°, for which S_{diff} splitting was determined from stacks. (c-d) are analogous to (a-b) but for δt.
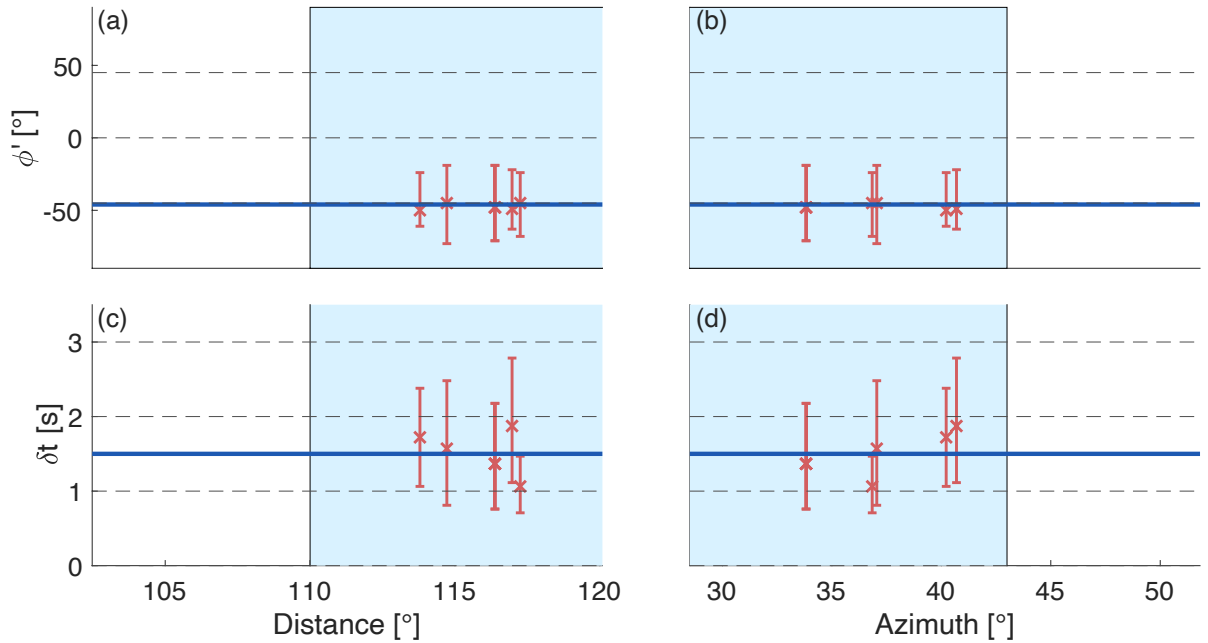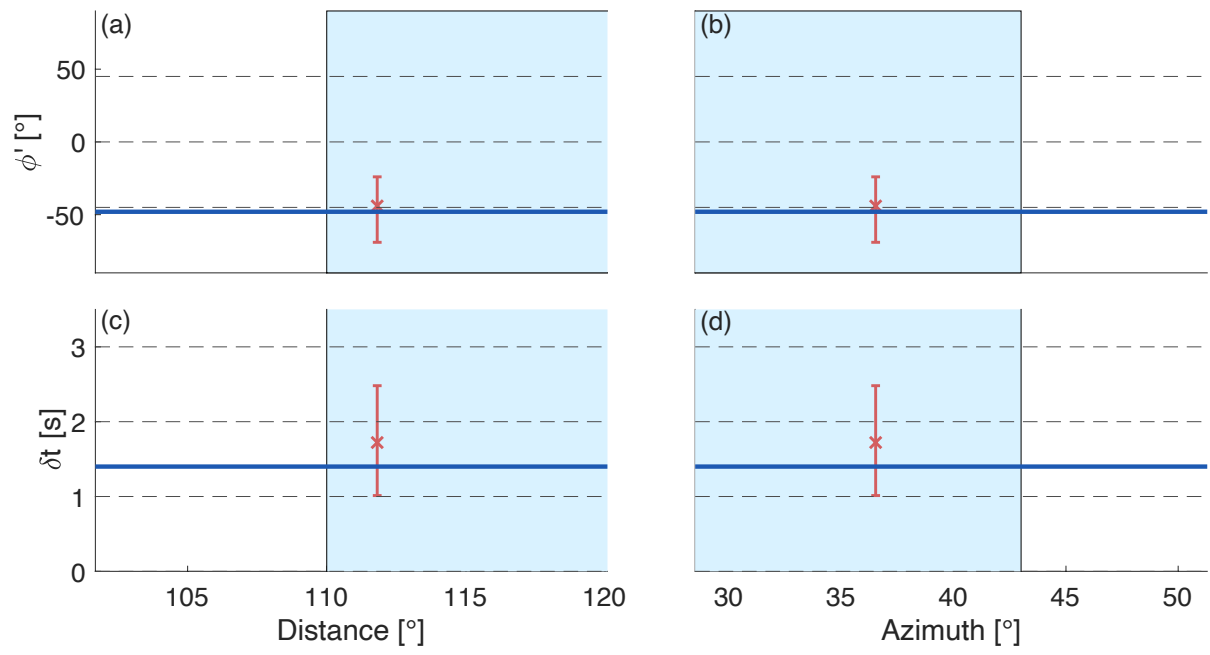

Figure S9: Like Figure S8 but for event 2009-10-07.
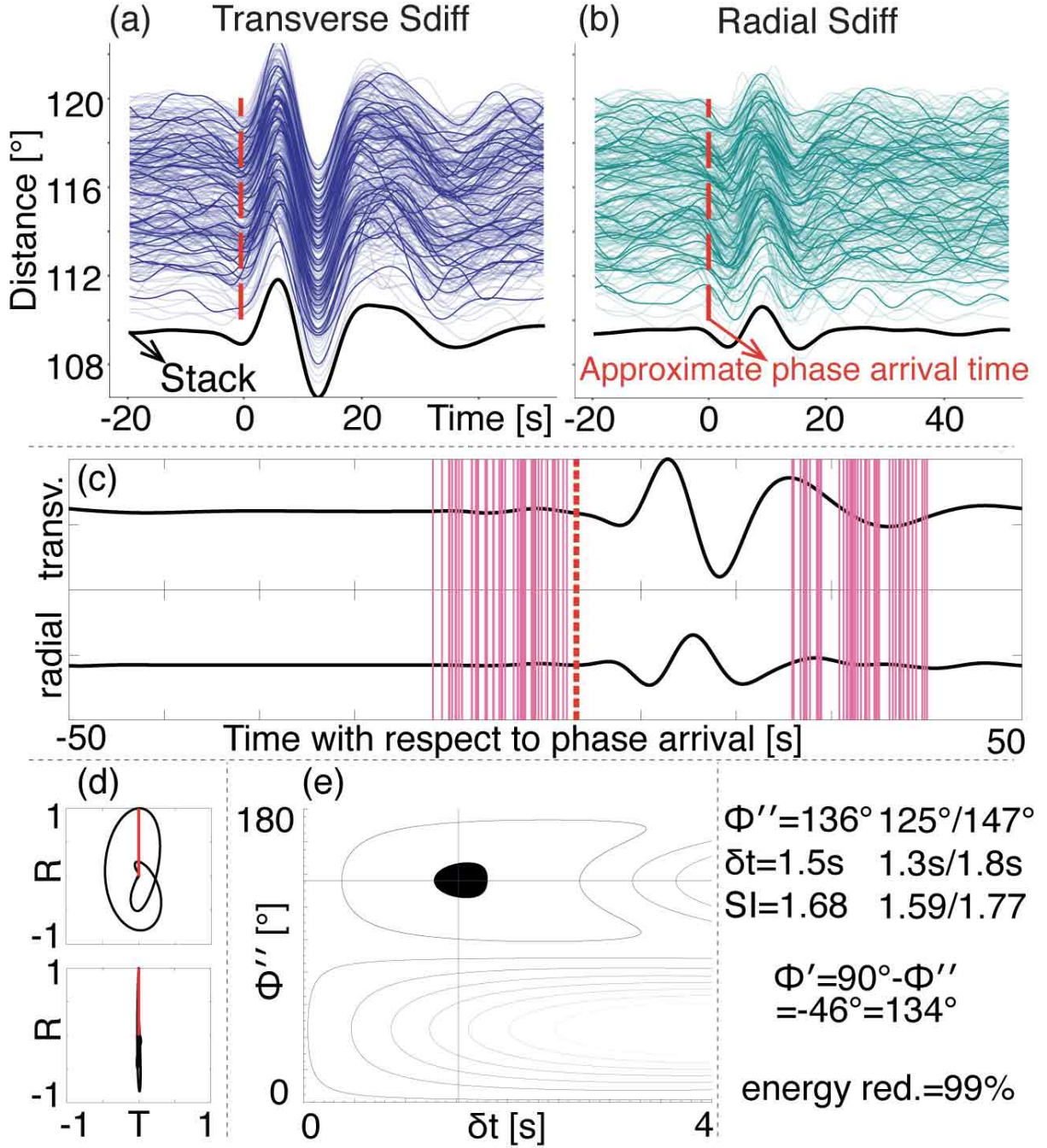
Figure S10: Like Figure S8 but for event 2010-10-24.

Figure S11: S$_{\text{diff}}$ waveforms and splitting diagnostic plots from SplitRacer for event 2009-10-07. In the waveform plots, approximate S$_{\text{diff}}$ arrival times are shown as a red dashed lines. (a) Transverse component waveforms recorded at a distance $> 110°$ and an azimuth $< 43°$ (see text). Waveforms were aligned and normalized with respect to the maximum transverse S$_{\text{diff}}$ amplitudes. (b) Similar representation of the corresponding radial S$_{\text{diff}}$ waveforms. Only every 10th trace is plotted without transparency to better visualize the individual waveforms. (c) Waveforms of the S$_{\text{diff}}$ stack (radial, top trace; transverse, bottom trace) are shown as black solid lines and the start/end of the 50 randomly chosen measurement windows as pink lines. (d) The upper diagram shows the particle motion for the original stack, the lower diagrams for the waveforms that were corrected for splitting. The red lines in the diagrams indicate the backazimuthal direction. (e) The best fitting splitting parameters are shown in the $\phi'' - \delta t$-plane, with black color indicating the 95% confidence region. For an explanation of the splitting parameters ϕ'' and ϕ' see Section 2.2 of the main manuscript.
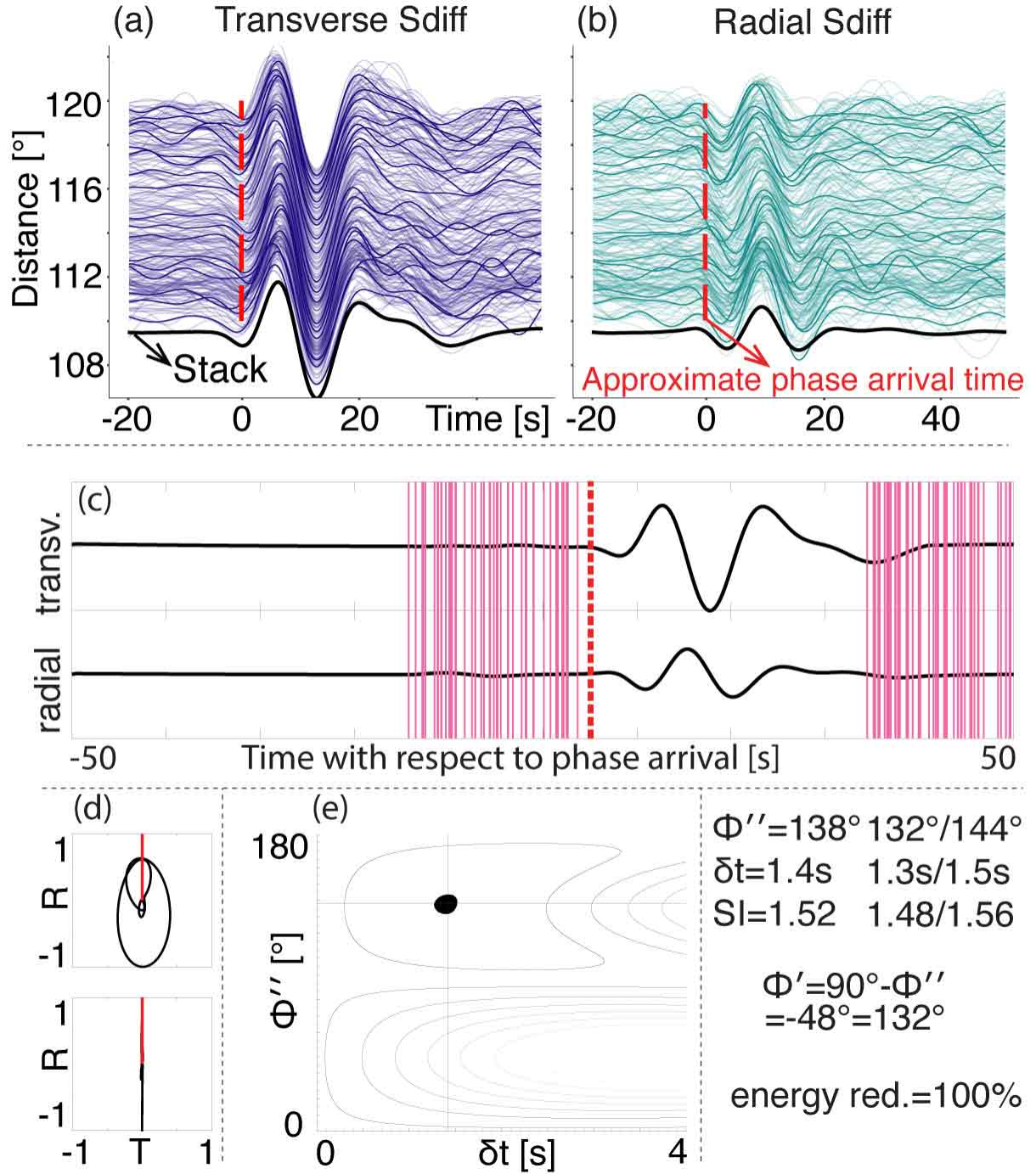
9

Figure S12: Same plotting conventions as in Figure S11 but here for event 2010-07-29.